

In vivo time-lapse imaging of mitochondria in healthy and diseased peripheral myelin sheath[☆]



Sergio Gonzalez^a, Ruani Fernando^a, Jade Berthelot^a, Claire Perrin-Tricaud^a, Emmanuelle Sarzi^a, Roman Chrast^b, Guy Lenaers^{a,c}, Nicolas Tricaud^{a,*}

^a INSERM U1051, Institut des Neurosciences de Montpellier, Université de Montpellier, Montpellier 34091, France

^b Karolinska Institutet, Department of Clinical Neuroscience, Department of Neuroscience, Stockholm 171 77, Sweden

^c Mitochondrial Medicine Research Centre, Pôle de Recherche et d'Enseignement en Médecine Mitochondriale, Université d'Angers, Angers 49933, France

ARTICLE INFO

Article history:

Received 23 February 2015

Received in revised form 26 May 2015

Accepted 26 May 2015

Available online 29 May 2015

Keywords:

Myelin

Schwann cell mitochondria

Opa1

Multiphoton microscopy

In vivo imaging

ABSTRACT

The myelin sheath that covers a large amount of neurons is critical for their homeostasis, and myelinating glia mitochondria have recently been shown to be essential for neuron survival. However morphological and physiological properties of these organelles remain elusive. Here we report a method to analyze mitochondrial dynamics and morphology in myelinating Schwann cells of living mice using viral transduction and time-lapse multiphoton microscopy. We describe the distribution, shape, size and dynamics of mitochondria in live cells. We also report mitochondrial alterations in Opa1^{delTTAG} mutant mice cells at presymptomatic stages, suggesting that mitochondrial defects in myelin contribute to OPA1 related neuropathy and represent a biomarker for the disease.

© 2015 Elsevier B.V. and Mitochondria Research Society. All rights reserved.

1. Introduction

Mitochondrial functions are essential for the maintenance of the nervous system. Indeed many neurodegenerative diseases such as Alzheimer's, Parkinson's, amyotrophic lateral sclerosis and peripheral nerve diseases involve dysfunctional mitochondria (de Moura et al., 2010; Cartoni and Martinou, 2009; Schroder, 1993). While the final outcome of these diseases is neuronal degeneration, previous data suggest a critical role for glial mitochondria in this process.

Indeed recent studies indicate that functional mitochondria are required in the myelin sheath to preserve axonal function and integrity (Viader et al., 2013). The myelin sheath covers a large amount of neurons both in the central (CNS) and the peripheral nervous system (PNS). Oligodendrocytes and Schwann cells in the CNS and PNS, respectively, wrap axons with multiple turns of compacted plasma membrane in order to electrically isolate successive axonal segments.

Abbreviations: mSC, myelinating Schwann cell; CMV promoter, cytomegalovirus promoter; OPA1, optic atrophy 1; AAV, adeno-associated virus; CAG promoter, cytomegalovirus beta-actin beta-globin promoter; ROI, Region of Interest; OPO, optical parametric oscillator.

[☆] The authors declare no competing financial interests.

* Corresponding author at: Institut des Neurosciences de Montpellier, 80, rue Augustin Fliche, 34091 Montpellier, France.

E-mail address: nicolas.tricaud@inserm.fr (N. Tricaud).

URL: <http://www.tricaud-lab.com> (N. Tricaud).

Each myelinated segment is separated from the next one by a node of Ranvier, where the machinery that allows the saltatory conduction of action potentials is concentrated (Eshed-Eisenbach and Peles, 2013). Mitochondria are abundant in the axon and they are enriched at nodes of Ranvier (Edgar et al., 2008; Ohno et al., 2011). These axonal mitochondria are crucial to repolarise the nodal membrane and therefore to maintain the nerve conduction.

The importance of mitochondria in the function of myelinated axons is further illustrated by the Charcot-Marie-Tooth peripheral nerve diseases that are due to mutations in genes involved in mitochondrial dynamics such as *GDAP1* and *MFN2* (Cartoni and Martinou, 2009; Cassereau et al., 2011). Intriguingly *GDAP1* has been involved both in axon-related disease CMT2K (Cassereau et al., 2011) and myelin-related disease CMT4A (Kabzińska et al., 2014), suggesting that mitochondria of both glia and axons are involved. Moreover mutations in OPA1 (optic atrophy 1), a gene essential for mitochondria fusion, were recently shown to give rise to systemic neurodegeneration including a peripheral neuropathy with features of axonal degeneration and demyelination (Bonneau et al., 2014; Yu-Wai-Man et al., 2010). Together these data indicate that glial and axonal mitochondria are central to the maintenance of the intimate axon–myelin relationship and the modulation of their physiology may provide an opportunity to treat peripheral nerve diseases.

However investigating the myelinating glia–axon relationship is not straightforward as it involves complex cellular interactions that are difficult to reproduce in vitro. Furthermore, while in vivo methods

have been developed to analyze mitochondrial dynamics in myelinated axons (Romanelli et al., 2013), the complementary technique for observing mitochondria in the surrounding myelinating Schwann cells (mSC) has not yet been described.

Here we detail a method to enable the visualization of mitochondria in myelinating glia in living mice using a multiphoton microscope. By contrast to existing published approaches to study axonal mitochondria (Misgeld et al., 2007), our method does not require engineered mutant mice and can therefore be directly applied to any mouse model of neuropathy. Moreover, this method allows longitudinal imaging for hours under physiological in situ conditions, without requiring nerve excision or displacement. Using this method, we show that presymptomatic OPA-1^{delITTAG} mice, mimicking human mitochondrial disease with peripheral neuropathy, display strong mitochondrial defects in their myelinating Schwann cells. This suggests that these mitochondrial defects can be used as a biomarker of the disease at presymptomatic stages and they may be the cause of the peripheral nerve disease.

2. Materials and methods

2.1. Cloning

pMito-dsRed2 (Clontech, Ref. 632421) was digested with NheI/NotI, blunted and cloned into pAdtrack-CMV (Quantum Biotechnologies, Inc.), pSICOR (Addgene, Ref. 11579) or pAAV-MCS (Cell Biolabs, Inc.) under the control of a CMV (pAdtrack-CMV, pSICOR) or a CAG (pAAV-MCS) promoter. Clones were validated by sequencing.

2.2. Viral particles production

Lentiviral and adenoviral production have been previously described in Gonzalez et al. (2014) and He et al. (1998) respectively. Briefly, to produce high-titer adeno-associated virus (AAV), three 15 cm dishes of 70–80% confluent HEK293T cells were transfected with 71 µg of pAAV expression vector, 20 µg of pAAV capsid and 40 µg of pHelper (Cell Biolabs, Inc.). The medium was collected two days after transfection, pooled and centrifuged 15 min at 2000 rpm to spin down floating cells. In parallel, cells were scraped, collected in PBS, lysed by 4 successive freeze–thaw cycles and centrifuged 15 min at 5000 rpm to discard cell debris. The cleared supernatant and the cleared medium were pooled and filtered with a 0.22 µm syringe driven filter. The viral solution was first filtered through a cation-exchange membrane Mustang S acrodisc (Pall Corporation) to remove empty particles and then through an anion-exchange membrane Mustang Q acrodisc (Pall Corporation) to retain infectious viral particles. Viral particles were then eluted in 10 mM bicine, 0.61 M NaCl, 2 mM MgCl₂ and 10% glycerol buffer and concentrated using centrifugal concentrators Amicon. This protocol routinely produced a titer of 10¹¹ PFU/ml. (for further details see Okada et al., 2009).

2.3. Mouse strains

Swiss mice (Janvier, France) were used for all experiments unless otherwise stated. The construction of the Opa1 knock-in mice with the recurrent OPA1 c.2708_2711delITTAG mutation was described in Sarzi et al. (2012). Experiments were carried out on 9 weeks old Opa1^{+/mut} (Opa1^{delITTAG}) mice and Opa1^{+/+} littermate controls. Mice were kept in the animal facility of the Institute for Neurosciences of Montpellier in clear plastic boxes and subjected to standard light cycles. All animal experiments were conducted in accordance with the French Institutional and National Regulation CEEA-LR-11032.

2.4. In vivo virus injection in the sciatic nerve

The protocol has been detailed previously (Gonzalez et al., 2014). Briefly, 6 weeks old mice were anesthetized and the incision area was

shaved and cleaned using betadine solution. After incision, the *gluteus superficialis* and *biceps femoris* muscles were separated to reveal a cavity crossed by the sciatic nerve. The nerve was gently lifted out using a fine spatula and a thin glass needle filled with viral solution (8 µl) was introduced into the nerve with a micromanipulator. This solution was injected over 30 min with short pressure pulses using a Picopump (World Precision Instrument) coupled to a pulse generator. After injection, the nerve was replaced into the cavity, the muscles were readjusted as before and the wound was closed.

2.5. Drug administration

Oligomycin A (Sigma, Ref. 75351) was stored in ethanol at 8 mg/ml and then diluted in 1 ml of sterile PBS at 80 µg/ml. The aqueous solution was warmed up to 37 °C for 10 min and 2 µl were injected into the mouse sciatic nerve using a Hamilton syringe. Alternatively the aqueous solution was diluted at 800 µg/ml in 3% low melting agarose solution and the drug-containing agarose solution was used to submerge the exposed nerve.

2.6. Immunohistochemistry

The dissected nerve was washed in L15 medium, fixed in Zamboni's fixative (Stefanini et al., 1967) for 10 min at room temperature, washed in PBS, and incubated in successive glycerol baths (15, 45, 60, 66% in PBS) for 18 to 24 h each before freezing at –20 °C. The nerves were cut in small pieces in 66% glycerol and the perineurium sheet removed. Small bundles of fibers were teased in double-distilled water on Superfrost slides, dried overnight at room temperature, and the slides stored at –20 °C. For immunostaining, the teased fibers were incubated for 1 h at room temperature in blocking solution (10% goat serum, 0.2% TritonX100, and 0.01% sodium azide in PBS). Then, the samples were then incubated with integrin-β1 primary mouse antibody (1/100, Chemicon, Ref. MAB1997), ATP synthase 1 primary mouse antibody (1/100, Life Scientific Thermo Fisher, Ref. A21351), PTEN primary rabbit antibody (1/200, Cell Signaling, Ref. 9188), ECCD2 primary mouse antibody (1/100, BD biosciences, Ref. 610181), Neurofascin primary rabbit antibody (1/500, abcam, Ref. 31457) or mito-Tracker Green TM (500 nM, Life technology, M-7514) in blocking solution overnight at 4 °C. The next day, the samples were washed in PBS and incubated for 1 h at room temperature with secondary donkey antibodies coupled to Alexa488 or Alexa647 (1/1600, Molecular probes, Ref. A21202 and 940076 respectively). Finally the samples were washed in PBS and mounted in Immuno-mount (Thermo Scientific). Images were acquired at room temperature using a 20× or 63× objective, a Zeiss confocal microscope LSM710, and its associated software.

2.7. Electron microscopy

WT and Opa1^{delITTAG} mouse sciatic nerves were fixed in situ in the cavity containing the nerve for 20 min with 4% PFA and 2.5% glutaraldehyde, in 0.1 M phosphate buffer (pH 7.3). Then nerves were removed and postfixed overnight in the same buffer. After washing 30 min in 0.2 M PBS phosphate buffer, the nerves were incubated with 2% osmic acid in 0.1 M phosphate buffer for 90 min at room temperature. Then, samples were washed in 0.2 M PBS phosphate buffer, dehydrated using ethanol gradient solutions and embedded in epoxy resin. For electron microscopy of sciatic nerves, ultrathin (70 nm) cross-sections were cut and stained with 1% uranylacetate solution and lead-citrate and analyzed using a HITACHI H7100 electron microscope at the 'Centre des Ressources en Imagerie Cellulaire' (CRIC) (for further details see Cotter et al., 2010).

2.8. Ketamine/xylazine anesthesia

1 ml of ketamine-HCl (100 mg/ml, IMALGEN, Merial Lab) and 0.1 ml of xylazine-HCl (100 mg/ml, ROMPUN, Bayer Sante) were mixed in a sterile tube with 8.9 ml of sterile PBS. The solution was kept away from light and stored at 4 °C. Then, mice were anesthetized using 0.1 ml of ketamine/xylazine solution per 10 g of body weight by intraperitoneal injection.

2.9. Sciatic nerve set up under multiphoton microscope

Three weeks after injection mice were anesthetized with a constant flow (1.5 l/min) of oxygen + 5% of isoflurane in an anesthesia box (World Precision Instruments, Ref. EZ-B800) for 5 min and after which the anesthesia was maintained with a mask delivering 2% isoflurane at 0.8 l/min. The incision area was shaved and cleaned, the skin was cut using a scalpel and the sciatic nerve was gently lifted out using a spatula. A flexible plastic bridge was gently inserted below the sciatic nerve and the nerve placed into a first chamber fixed to the bridge. At that point the mouse was placed under the multiphoton microscope, the bridge was fixed using magnetic brackets to minimize/eliminate physiological movements and mouse legs were fixed in place with clamps. The first chamber and the nerve were then submerged with a solution of 3% low melting agarose (Promega) diluted in Leibovitz's L15 medium (Gibco Life Technologies) and maintained at 37 °C. Immediately, a second chamber (MatTek Corporation, Ref. P35G-0-14C) was fixed on the top of the first chamber and on the nerve using a drop of agarose solution carefully avoiding the formation of air bubbles. When the agarose was hard, the upper chamber was filled with deionized water to immerse the 63× objective lens (Carl Zeiss Microscopy, LD C-Apochromat, Ref. 421887-9970).

2.10. Multiphoton image acquisition

All time-lapse images were obtained with a multiphoton microscope LSM 7 MP OPO (Zeiss, France) coupled to a dark microscope incubator (L S1 Dark, Zeiss) in which the temperature was maintained at 37 °C (Heating Unit XL S, Zeiss, France). Mitochondria images were acquired by time-lapse recording one image every five minutes during five (live animals) to sixteen hours (dead animals). Each image is a stack of 10 scans over 20 μm depth. Each scan was acquired at constant laser intensity (1%) during 100 ms with a 512 × 512 pixel resolution. Images, acquired with ZEN software (Zeiss), were saved in .czi format and processed using Image J software.

2.11. Data and statistical analysis

To measure mitochondrial speed we defined a Region of Interest (ROI) encompassing each mitochondrion using Image J and the movement of every ROI was calculated using the Multitracker plugin of Image J software and then represented as μm displacement per minute (Supplementary Fig. 1). To measure mitochondrial size we drew a line along the longest axis of every isolated mitochondrion and measured the line length using Image J software. Finally the ratio of mitochondrial fusion and fission events were calculated by manually counting isolated mitochondria extremities at time(h) = t expressed over the number of extremities at time(h) = t - 1 (percentage of fusion-fission events over 1 h). In order to measure mitochondrial object number, diameter and area, microscope imaging parameters were maintained over all different regions we imaged (Supplementary Fig. 2). The data are shown as the mean ± SEM. Statistical significance was determined using a two-tailed Student's *t* test and ANOVA. Significance was set at * and #*P* < 0.05, ** and ##*P* < 0.01, or ****P* < 0.001. *n* represents the number of independent experiments.

3. Results

3.1. Virally-delivered mito-dsRed2 selectively labels mitochondria in mSC in vivo

Viral particles expressing the mito-dsRed2 protein were produced using HEK293T cells, purified and concentrated before to be injected into 6 week-old mouse sciatic nerve as described previously (Gonzalez et al., 2014) in order to infect mSC in vivo. Indeed our previous studies have shown that viral vectors can be used to specifically transduce mSC in the sciatic nerve of living mice (Gonzalez et al., 2014; Tricaud et al., 2005). Three weeks later animals were sacrificed, the injected sciatic nerves fixed for immunohistochemistry and myelinated fibers teased on a glass slide. Using confocal microscopy we observed that mito-dsRed2 labeled discrete structures in mSC (Fig. 1a). At higher magnification and on a single confocal plan, these structures were circular or tubular (Fig. 1b) with a mean diameter of 0.38 μm ± 0.13 (Fig. 1c), which is consistent with the morphology and size of the labeled mitochondria as indicated in previous reports (Bereiter-Hahn and Vöth, 1994). Moreover these mito-dsRed2 labeled structures colocalized with typical mitochondrial markers such as MitoTracker (Fig. 1d) and ATP synthase (Fig. 1e). Taking together these data indicate that mito-dsRed2 specifically labels mitochondria in mSC in vivo.

3.2. Distribution of mitochondria in mSCs

While the morphology of mitochondria in mSC have been well described by electron microscopy, the imaging of these organelles using light microscopy has been hindered by the fragility of these small structures and the relative weak fixation required for immunostaining. To show the distribution of labeled mitochondria in mSC we used immunostaining and identified the different myelin sheath subdomains: E-cadherin2 labels the Schmidt-Lanterman incisures, the paranodal loops and the inner and outer edges of the myelin (Tricaud et al., 2005), PTEN labels the adaxonal domain of the myelin (close to the axon) (Ozçelik et al., 2010), β1-Integrin labels the abaxonal membrane and Cajal's bands (opposite to the axon) (Ozçelik et al., 2010) and neurofascin labels paranodal loops and the node of Ranvier (Zonta et al., 2008). So using virally-delivered mito-dsRed2 and confocal microscopy we visualized the heterogeneous distribution of mitochondria in the myelin sheath (Figs. 1a and 2) reflecting the distribution previously described with electron microscopy imaging. Indeed mitochondria were mostly localized in paranodal regions (Fig. 2b and c), in the Cajals bands (Fig. 2d and e), around the nucleus (Fig. 2f and g) and at the outside edge of incisures (Fig. 2h and i). In these regions mitochondria were abundant both in paranodal loops close to the axolemma (Fig. 2j and k) and in the deep cytoplasmic indentations that characterize paranodal myelin (myelin crests) (Fig. 2b and c). When we measured mitochondria number, diameter and area along the full myelin sheath, we observed that mitochondria were more abundant and bigger around the nucleus and at paranodal regions (Fig. 2l and m). This paranodal abundancy was previously described using electron microscopy and the indented paranodal cytoplasmic regions in myelin were defined as "mitochondrion bags" (Berthold and Rydmark, 1995).

3.3. A reliable multiphoton microscope set up for live mSC mitochondria imaging

While electron microscopy is the method of choice to observe the structure of mitochondria, it provides only limited information about the physiology and the behavior of these organelles in living cells. With the aim to address these questions we developed a multiphoton microscope set up to observe mitochondria in living mSC in vivo (Fig. 3a). Briefly, three weeks after mSC mitochondria labeling through viral injection, the mouse was anesthetized and its intact sciatic nerves

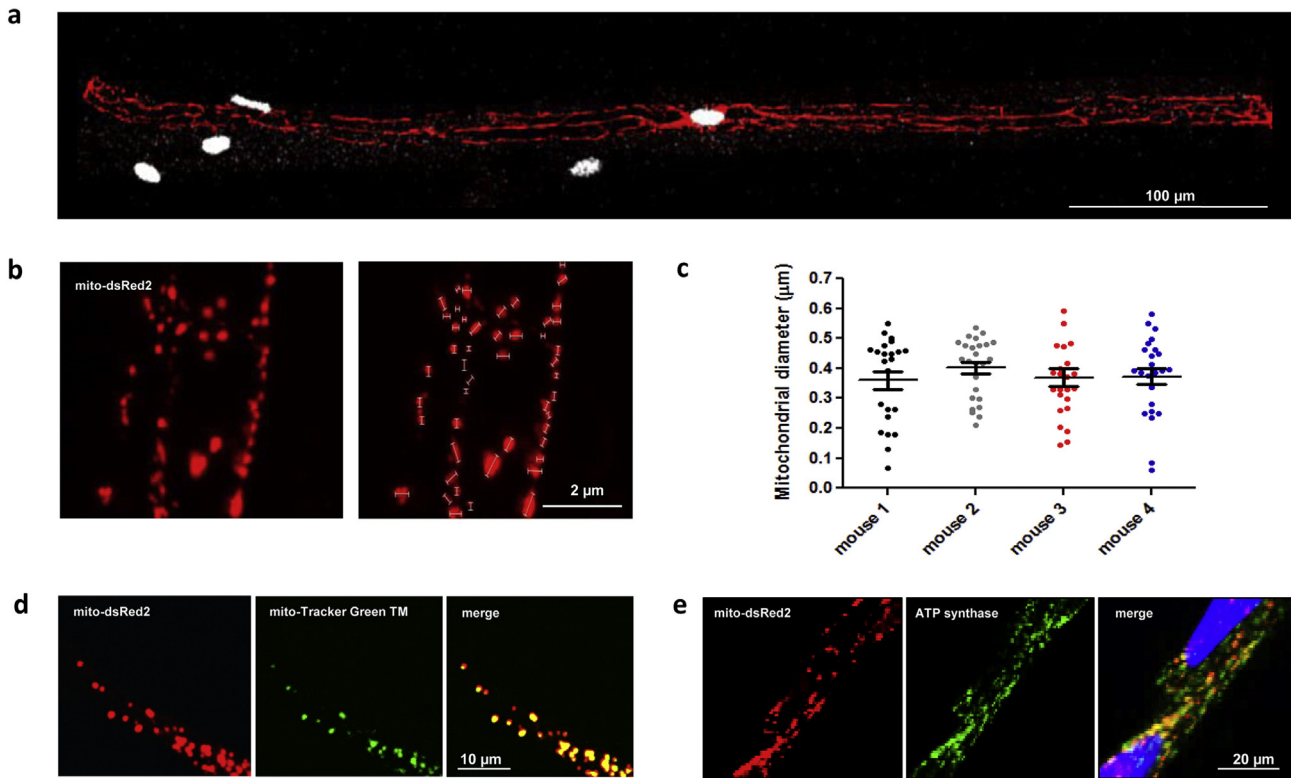


Fig. 1. Virally-delivered mito-dsRed2 selectively labels mSC mitochondria. (a) Representative image of mSC infected with viral particles expressing mito-dsRed2 protein (red). The cell nucleus is labeled with DAPI (white). Scale bar: 100 μm . (b) Representative image of mitochondrial diameter quantification using longitudinal image of mito-dsRed2 infected mSC. Scale bar: 2 μm . (c) Mitochondrial diameter quantification of mito-dsRed2 infected mSC. Only isolated mitochondria were quantified. Mean mitochondrial diameter: $0.38 \mu\text{m} \pm 0.13 \text{SD}$. $n = 4$ mice, approx. 100 mitochondria. Scale bar: 2 μm . (d) Viral particles expressing mito-dsRed2 selectively labels mitochondria. mSC infected with a virus expressing mito-dsRed2 (red), labeled with Mito-Tracker Green TM (green) and merge (yellow). Scale bar: 10 μm . (e) mSC infected with a virus expressing mito-dsRed2 (red), immunostaining for mitochondrial ATP synthase (green) and merge (yellow). Scale bar: 20 μm .

was placed in a first chamber embedded in agarose (Fig. 3b, c and e). A second chamber filled with water was mounted on top of the first one in which the microscope objective lens was immersed (Fig. 3d and e).

While confocal microscopy is the tool of choice when working with highly fluorescent and fixed samples, it is much less useful for live samples as it induces phototoxicity and the light penetration deep in the sample is limited. Instead multiphoton microscopy using light with higher wavelengths and allowing a better focus of the illuminating beam is ideal for in vivo imaging (Christensen and Nedergaard, 2011). We next set-up the optimal imaging conditions with a multiphoton microscope LSM 7 MP OPO (Zeiss, France). We observed that dsRed2 fluorescent probe can be excited at 750 nm and also at 920 nm using biphotonic laser (Marchant et al., 2001). However we observed a strong photobleaching after two hours of image capture (every 5 min) at 750 nm, but not at 920 nm excitation light (Fig. 4a). Thus the 920 nm wavelength was used for excitation in all following experiments.

Using the above described multiphoton microscope we were able to follow mitochondria in mSCs for up to 5 h in vivo. Indeed we found mitochondria to be highly motile but surprisingly most of these organelles did not travel but oscillated around themselves. Indeed less than 5% of the mitochondria moved more than 3 μm away from their initial position during 10 min. We quantified these oscillation-like movements, the mitochondrial size and fusion–fission events (Figs. 4 and 5). All these parameters remained constant over the 5 h of imaging suggesting that we were able to follow the behavior of mitochondria in mSCs of living mice without affecting their physiology. Moreover we found that these parameters were quite homogenous along the mSC domains, from one cell to another and from one animal to another, further suggesting that we are observing “normal” mitochondria behavior in mSC of living mice. In addition the strain of the mice examined did

not have a significant impact on these parameters (data not shown). Finally, we also verified whether isoflurane anesthetic altered mitochondrial physiology in our in vivo system, as reported in vitro (Hirata et al., 2011). We repeated the experiments with mice anesthetized using intraperitoneal injections of ketamine/xylazine, a cocktail that has no reported effect on mitochondria. No significant difference could be detected on all parameters between the two anesthesia methods (Fig. 4e–g), showing that isoflurane did not generate artifacts under our experimental conditions.

We were able to reliably image live animals under anesthesia for approximately 5 h. After five hours, the death of the animals, due to the long anesthesia procedure, lead to a rapid decrease in mitochondria motility and a reduction in mitochondrial size (Fig. 4b–d; Video 1), showing that the parameters recorded in living animals were characteristic/indicative of healthy mitochondria under physiological condition. Therefore, for the rest of study we used these typical changes in parameters (e.g. decrease in mitochondria motility and a reduction in mitochondrial size) as a mark of mSC death.

3.4. Changes in mitochondrial parameters correlate with alteration of mitochondria physiology and with mitochondrial diseases in peripheral nerves

We next investigated glial mitochondria physiology under disease-relevant in vivo conditions. First we tested whether the in vivo measured mitochondrial parameters are changed when mitochondria physiology is altered. An increasing number of drugs are known to disrupt mitochondrial functions, some of them leading to peripheral neuropathy (Cornblath and Hoke, 2006; Feldman and Anderson, 1994). We decided to use oligomycin A, an antibiotic that inhibits mitochondrial ATP production (Lardy, 1980) in order to change mitochondrial physiology

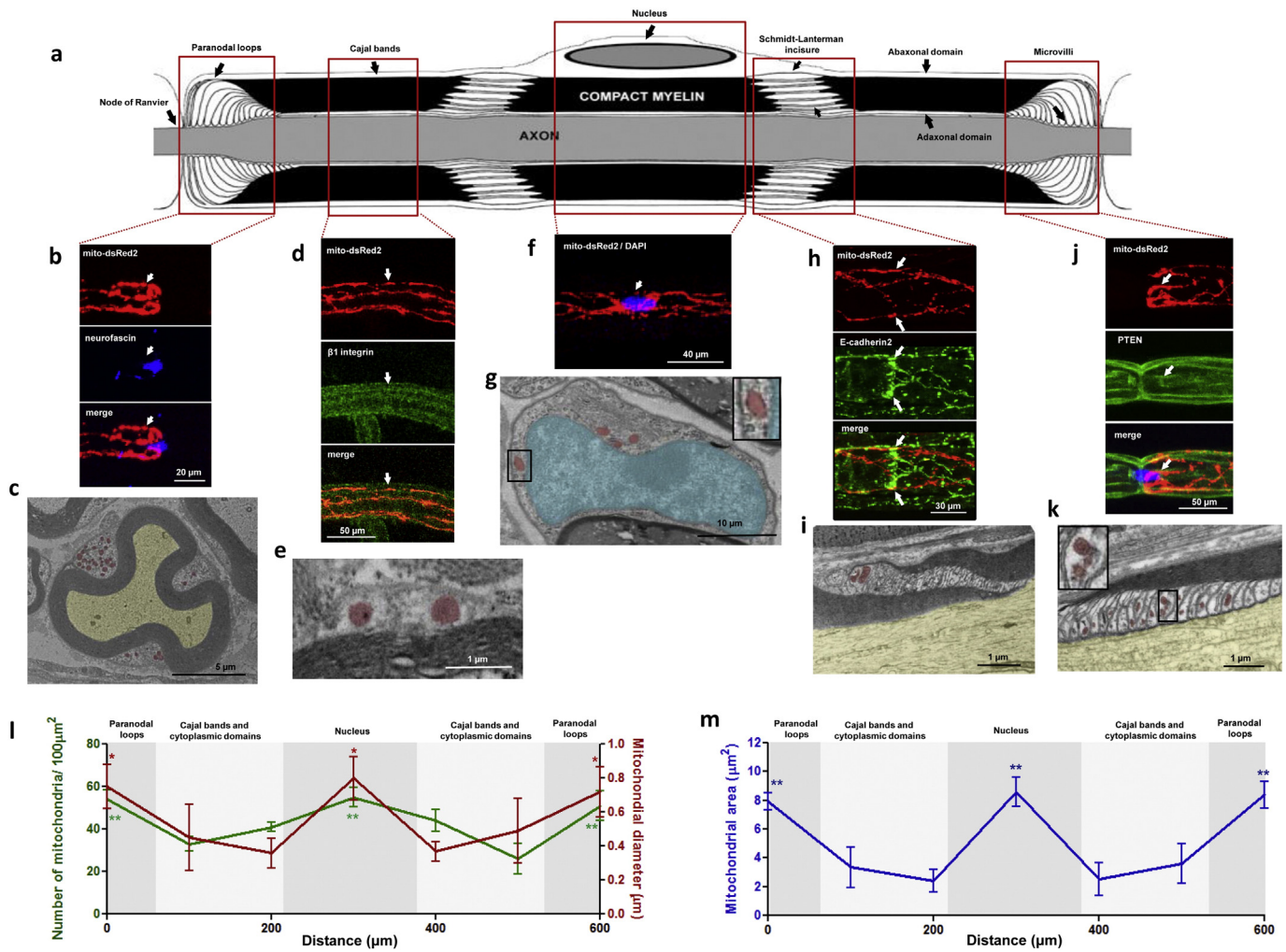


Fig. 2. Mitochondria morphology and distribution in mSC. (a) Schematic drawing of various cellular domains present in mSC (top panel). Red frames highlight the different mSC domains. In middle panels, representative immunostaining images of mitochondria distribution and morphology in the different mSC domains using immunostaining or transmission electron microscopy (TEM). Mito-dsRed2 labeled mitochondria are shown in red. The following markers of various mSC domains (in green) were used: β 1-integrin labeling the abaxonal membrane (d), E-cadherin2 labeling Schmidt–Lanterman incisures and paranodal loops (h) and PTEN labeling cytoplasmic adaxonal domains (j). In blue neurofascin labeling shows the paranodes and the node of Ranvier (b) and DAPI labeling shows the nucleus (f). White arrows mark cell domains indicated in the schematic drawing. In bottom panels, transversal (c, e and g) or longitudinal (i and k) TEM images of mSC at the respective regions of the myelin sheath. Mitochondria are artificially colored in red, nucleus in blue and axon in yellow. Each immunostaining and TEM experiment was repeated at less 5 times of 5 independent mice. Axonal mitochondria never expressed mito-dsRed2. (l) Number of mitochondria (green), mitochondrial diameter (red) and (m) mitochondrial area (blue) quantification along the mSC domains. Error bars indicate SEM. $n = 12$ mSC of 12 different mice. Asterisks mark statistical differences compared to Cajal bands mitochondria number and diameter. Statistical significances were determined using a two-tailed Student's *t* test. Statistical differences: * $P < 0.05$ and ** $P < 0.01$.

in vivo. We injected 2 μ l of 80 μ g/ml oligomycin A into mito-dsRed2 infected mouse sciatic nerves just before imaging. Oligomycin A induced a fast decrease of mitochondrial movements (Fig. 5a red line; Video 2) a significant reduction of fusion and fission events (Fig. 5b) and a decrease of mitochondrial size (Fig. 5c and d). Interestingly, equivalent results were obtained, albeit with a 2 h delay when the drug was supplemented, at 10X concentration, in the agarose surrounding the nerve (Fig. 5a blue line; Video 3). These results are consistent with the known effects of oligomycin A on mitochondrial speed, size and fusion–fission (Legros et al., 2002) and indicates that physiological changes occurring in Schwann cell mitochondria can be detected in real time in vivo.

Mutations in OPA1 gene were originally recognized as responsible for dominant optic atrophy, an inherited disease affecting the optic nerve integrity (Delettre et al., 2000). OPA1 encodes a pro-fusion mitochondrial dynamin-related GTPase located in the inner membrane that is involved in many mitochondrial functions, notably in the maintenance of the respiratory chain and membrane potential (Olichon et al., 2003; Lodi et al., 2004; Amati-Bonneau et al., 2005), control of apoptosis

(Olichon et al., 2003; Frezza et al., 2006) and mitochondrial DNA maintenance (Amati-Bonneau et al., 2008; Elachouri et al., 2011). Recently we generated a new Opa1^{delTTAG} mouse model of optic atrophy, closely mimicking the complex phenotype of the human disease (Sarzi et al., 2012), and showed that OPA1 mutation not only induces optic nerve defects but affects also the peripheral nervous system (Amati-Bonneau et al., 2009; Sarzi et al., 2012). Indeed the demyelination features in these mice start at 5 months of age (Fig. 5e) increasing in severity with age. Electron microscopy imaging of mitochondria in the peripheral myelin of Opa1^{delTTAG} mutant mice did not reveal any change in the mitochondrial diameter (Fig. 5f and g). Moreover when we labeled mutant mice mitochondria with virally-delivered mito-dsRed2 no change could be detected in mitochondrial diameter measured by in vivo multiphoton imaging (Fig. 5h) or the distribution of the mitochondria along the myelin sheath (Fig. 5i). To go further we quantified in vivo mitochondrial movements, size and fusion–fission by time-lapse recording (Videos 4 and 5). Similar to our data obtained after oligomycin A treatment (Fig. 5a), we observed a significant and steady decrease in mitochondrial motility

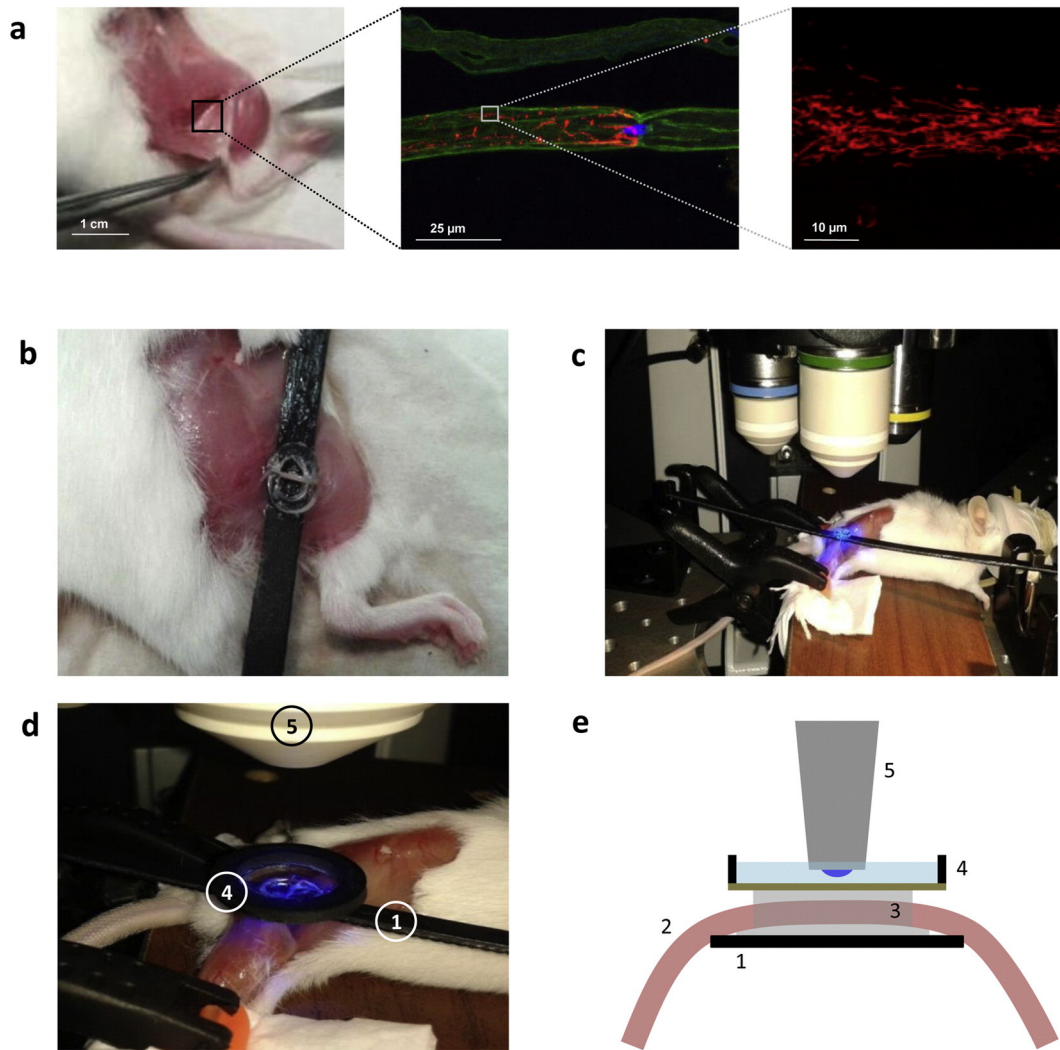


Fig. 3. Multiphoton microscope set up for mitochondrial imaging in mSC of the mouse sciatic nerve. (a) Schematic overview of the imaging approach. Left panel: The sciatic nerve is shown after skin incision and muscle displacement. Middle panel: Confocal microscopy images of a mSC immunostained for integrin- β 1 (green) show mitochondria labeled with mito-dsRed2 (red) after viral transduction in vivo. In blue neurofascin labeling of paranodes and node of Ranvier. Right panel: a higher magnification image shows mito-dsRed2 labeled mitochondria (red) in a Schwann cell in vivo using multiphoton microscope. (b) After skin incision and muscle displacement, the mouse sciatic nerve is lifted out and placed in a 4 mm wide chamber using a flexible black plastic bridge. (c) The mouse is placed under the multiphoton microscope objective. Mouse legs are gently immobilized using forceps and the bridge is stabilized using magnetic brackets. (d) A second glass bottom chamber dish (15 mm wide) is glued to the first chamber using agarose low melting 3% solution and then filled with sterile water to accommodate the immersion objective. 1: Flexible plastic bridge, 4: second chamber filled with water and 5: microscope objective lens. (e) Schematic drawing of mouse multiphoton set up. 1: Flexible plastic bridge, 2: sciatic nerve, 3: first chamber filled with agarose, 4: second chamber filled with water and 5: microscope objective lens.

(Fig. 5j gray line) over the course of five hours, showing that this effect was not due to cell death. This decrease in motility was coupled to a strong reduction of fusion but not fission events (Fig. 5b gray bars), which contrasted with the effects of oligomycin A on both parameters (Fig. 5b red bars). This indicated a role for OPA1 in fusion events, which is consistent with the known in vitro function of the protein (Belenguer and Pellegrini, 2013). Finally we found a strong reduction in mitochondrial length (Fig. 5c and d), which was more pronounced than oligomycin A treatment (Fig. 5d red bars). Taken together these data show that while the overall structure and the distribution of mitochondria are not affected by OPA1 dysfunction, the motility and, more significantly, the fusion process and the size of mitochondria are impaired. Moreover it shows that the in vivo imaging of mitochondria is essential to detect mitochondrial changes that are not or hardly detectable using classical electron microscopy studies. In addition as these defects were detected in 9 weeks old Opa1^{delTTAG} mutant mice, well in advance of the first reported symptoms or peripheral nerve defects (Sarzi et al., 2012), it is likely that the impairment of

mitochondria in Schwann cells precedes and may contribute to the pathology of peripheral nerve disease in this mouse model.

4. Discussion

Here, we present a new technique to analyze in vivo mitochondria dynamics and morphology in mSC of the peripheral nervous system using viral particles expressing fluorescent probes and time-lapse multiphoton imaging. Notably, this method does not require mice genetically engineered to express fluorescent probes and can therefore be directly applied on any mutant or pharmacology induced model of neuropathy, as demonstrated through characterization of Opa1^{delTTAG} mutant mice.

The use of mito-targeted fluorescent probes expressed in only a few cells, via the viral transduction technique, is essential to limit the labeling of all mitochondria in the nerve as seen with fluorescent mito vital dyes (Romanelli et al., 2013). Indeed the general labeling of mitochondrial both in axons and in glia generates a high fluorescent

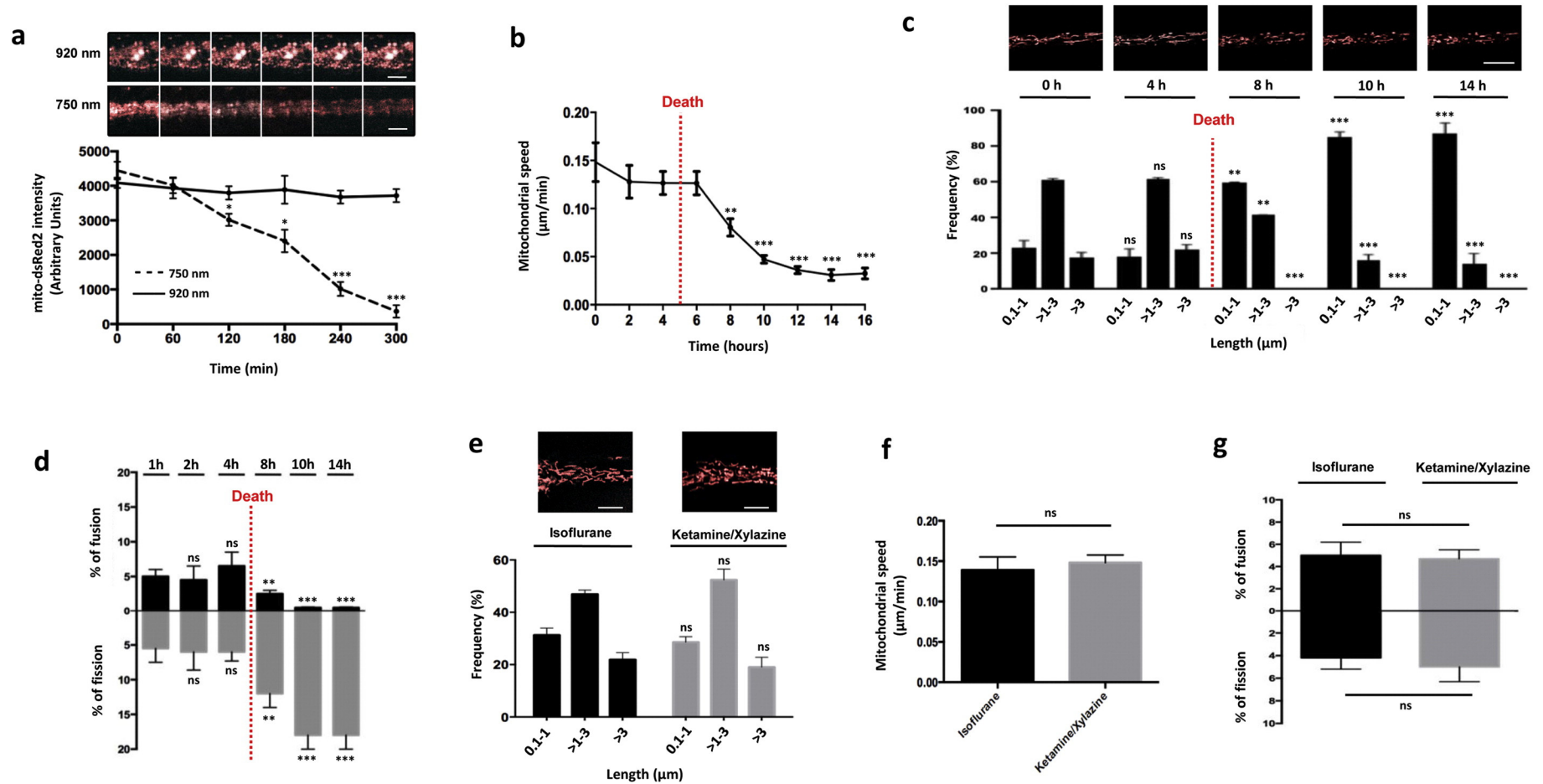


Fig. 4. *In vivo* analysis and validation of mSC mitochondria dynamics and morphology. (a) Top panels: Images showing mito-dsRed2 intensity after excitation at the two different wavelengths indicated during 5 h of time-lapse in living image acquisition using $63\times$ objective and 1% of laser intensity. Scale bar: $1\ \mu\text{m}$. Lower panel: quantification of the signal intensity over time. Continuous and discontinuous lines represent data obtained for 920 nm and 750 nm wavelength excitations respectively. Statistical analysis compared intensity at $T = 0$ min for each wavelength. (b) The motility of mito-dsRed2 labeled mitochondria in virally-transduced Schwann cells was measured over 16 h and plotted as mitochondrial speed over time. After five hours of imaging we consistently observed that animal breathing movements stopped and anesthetized mice died (red dotted line). This was followed by a slow down of mitochondria movements. Statistical analysis (marked by asterisks) compares mitochondrial speed at $T = 0$ h with subsequent time points. (c) Top panels: images illustrating mitochondria morphology at the different time points. Scale bar: $5\ \mu\text{m}$. Bottom panel: Mitochondrial length distribution frequency at different time-points showing a progressive fragmentation of mitochondria. Statistical analysis compares the frequency of each length range at $T = 0$ h with subsequent time points. (d) Ratio of mitochondrial fusion and fission events over time. Statistical analysis compares percentage fusion/fission at $T = 1$ h with subsequent time points. (e) Top panels: images illustrating mito-dsRed2-labeled mitochondria using isoflurane or ketamine/xylazine anesthesia. Scale bar: $5\ \mu\text{m}$. Lower panel: Mitochondrial length distribution frequency in Schwann cells of mice anesthetized with isoflurane (black bars) or ketamine/xylazine (gray bars). No significant difference was found between the two anesthesia methods. (f) Mitochondrial speed in mice anesthetized with isoflurane (black bar) or ketamine/xylazine (gray bar). (g) Ratio of mitochondrial fusion and fission events in mice anesthetized with isoflurane (black bar) or ketamine/xylazine (gray bar). Error bars indicate SEM. $n = 3$ to 6 mice. ns: non-significant, statistical differences: * $P < 0.05$, ** $P < 0.01$, *** $P < 0.001$.

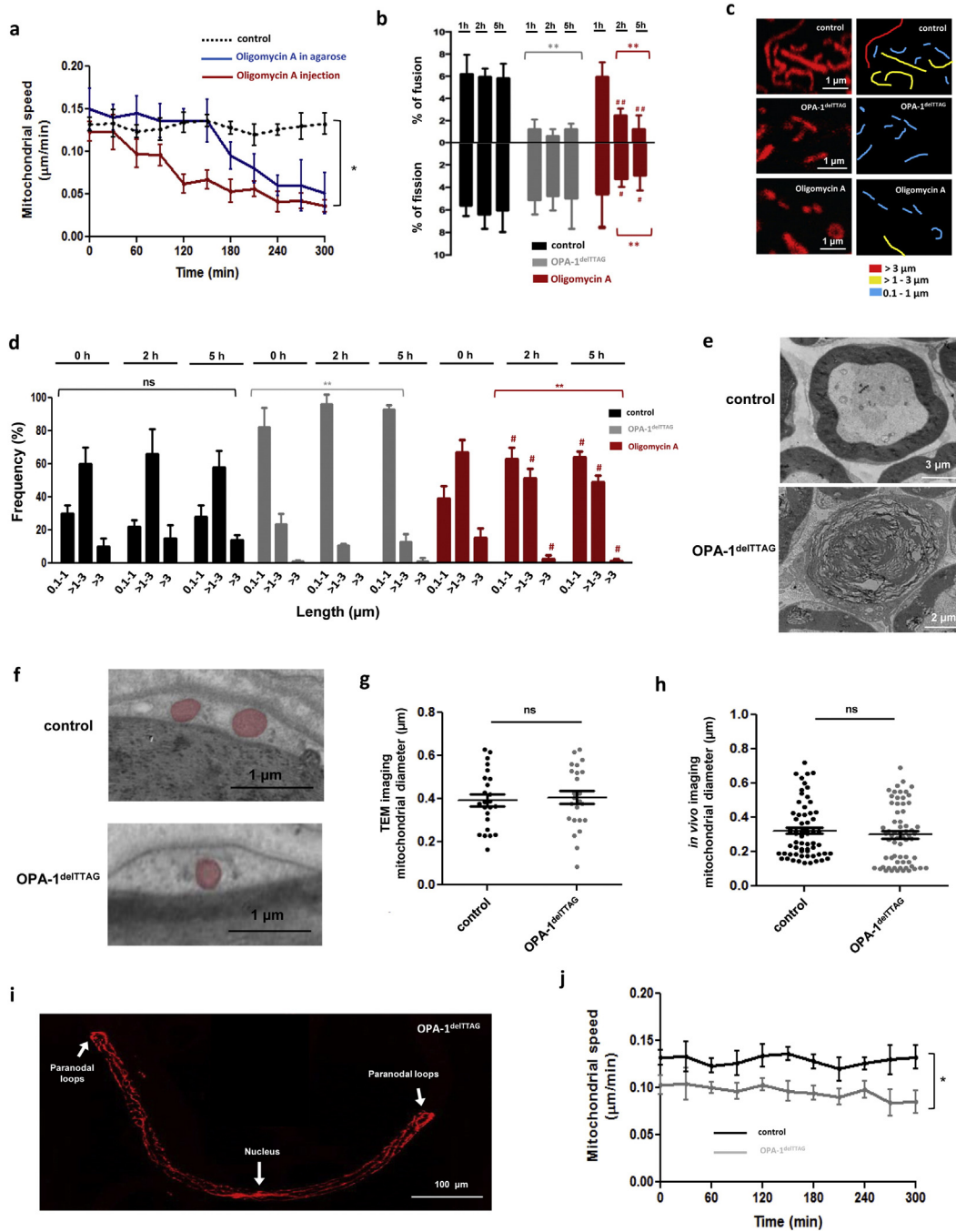


Fig. 5. *In vivo* mitochondrial dynamics and morphology analysis of OPA1 peripheral neuropathy model and drug treatment. (a) mSC mitochondrial speed of control (discontinuous black line) and mice treated with oligomycin A injected into the nerve (red line) or applied topically in the agarose (blue line) along 5 h of time-lapse acquisition. Asterisks mark statistical differences relative to control mice at T = 300 min. (b) Ratio of mitochondrial fusion and fission events in control mice (black bars), Opa1^{delITTAG} mice (gray bars) and wild type mice treated with oligomycin A injected into the nerve (red bars). Asterisks and hashes mark statistical differences compared to control mice or basal conditions (T = 0 h) respectively. (c) Representative *in vivo* mitochondria images (left panels) and mitochondria length quantification (right panels) of control, Opa1^{delITTAG} and oligomycin A treated mice after 5 h of time-lapse imaging acquisition. Scale bar: 1 μ m. In red mitochondria size > 3 μ m, in yellow mitochondria size > 1–3 μ m and in blue mitochondria size between 0.1 and 1 μ m. (d) Mitochondrial length frequency distribution in control mice (black bars), Opa1^{delITTAG} mice (gray bars) and wild type mice treated with oligomycin A injected into the nerve (red bars). Asterisks and hashes mark statistical differences compared to control mice or basal conditions (T = 0 h) respectively. Error bars indicate SEM. n = 4 to 6 mice. ns: non-significant statistical differences: * and # P < 0.05, ** and ## P < 0.01. (e) Myelin sheath structure of 9 months old control (top panel) and Opa1^{delITTAG} mouse (bottom panel) mSC. (f) TEM image of mSC 5 months old control (top panel) and Opa1^{delITTAG} mice (bottom panel). Mitochondria are artificially colored in red. (g) Mitochondrial diameter quantification using TEM images of control and Opa1^{delITTAG} mice. Error bars indicate SEM. n = 25 mitochondria each group. ns: statistically non-significant difference. (h) Mitochondrial diameter quantification using *in vivo* multiphoton imaging of control and Opa1^{delITTAG} mice. Error bars indicate SEM. n = 65 mitochondria in each group. ns: statistically non-significant difference. (i) Representative image of 5 months old Opa1^{delITTAG} mice mitochondria distribution along the myelin sheath. White arrows mark paranodal loops and cell nucleus. Scale bar: 100 μ m. (j) Mitochondrial speed in control mice (black line) and Opa1^{delITTAG} mice (gray line) along 5 h of time-lapse *in vivo* imaging acquisition. Asterisk marks statistical differences relative to control mice at T = 300 min.

background that strongly hinders the imaging (data not shown). In addition the viral delivery technique is a fast and efficient alternative to the creation of transgenic mouse lines expressing fluorescent probes

in cells of interest, thus enabling existing mutant mice disease models to be easily analyzed for mitochondrial dysfunctions. Our approach also takes advantage of the accessibility and the elasticity of the sciatic

nerve to expose it under an objective while limiting the perturbations resulting from breathing movements. Finally the method incorporates the use of an agarose filled chamber to submerge and immobilize the nerve while maintaining it under physiological conditions. This chamber can also be exploited to deliver drugs to living Schwann cells and axons while simultaneously visualizing the consequences on mitochondrial physiology. Therefore this method may be very useful to test in vivo the effects of drugs designed to treat peripheral nerve diseases, to block degeneration or to promote regeneration.

Using this novel method we have confirmed the wide distribution of mitochondria along the myelin sheath previously described using electron microscopy (Berthold and Rydmark, 1995). Moreover we have shown that mitochondria are more abundant in the perinuclear cytoplasm and in paranodal loops where they localize both in the inner adaxonal part and in the outer abaxonal part. This enrichment in paranodal loops is interesting because axonal mitochondria have been shown to be abundant in paranodes (Zhang et al., 2010), where an unclear mechanism appears to sequester them (Einheber et al., 2006). So this suggests that glial and axonal mitochondria may functionally or metabolically interact in these paranodal regions, where they are more closely localized.

We then used the full potential of the method to analyze mitochondria in mSC in vivo. As observed in other cell types in vivo and notably in peripheral neurons (Misgeld et al., 2007), most of the organelles did not travel long distances but instead oscillated around their origin. This movement requires ATP production as the inhibition of ATP synthase by oligomycin A strongly impaired the phenomenon. This is consistent with recent data showing that the movements of mitochondria on microtubules require ATP hydrolysis (Cai et al., 2011). Oligomycin A also affected both fusion and fission events suggesting that both events require ATP hydrolysis too. Moreover as these opposite processes were affected in a similar way, long mitochondria fragmented but the overall fragmentation was less severe than in Opa1^{delTTAG} mutant mice, where only fusion was affected. It is worth noting that mitochondrial parameters were remarkably homogenous between cells and animals, strongly supporting the assumption that we observed physiological mitochondrial dynamics in vivo.

We then investigated a syndromic mitochondrial disease recently elaborated by a new Opa1^{delTTAG} mutant mouse model and we provide new insight into the pathophysiology on this disease. We observed that this mouse model had uniformly reduced mitochondrial movements suggesting that ATP synthesis is impaired by OPA1 dysfunction. This movement defect was less severe compared to nerve treated with oligomycin A suggesting that OPA1 dysfunction may affect mitochondrial movement by other means. The major effect of this mutation was the impairment of the mitochondrial fusion process. As the fission process remained unchanged the fragmentation of mitochondria was maximal in comparison with oligomycin A treatment. We could not detect the impact of the fusion defect on the distribution of the organelles in the myelin or on the structure of the mitochondria. Moreover at 9 weeks postnatal, the age of the mice analyzed in this study, no myelin defect was observed in the mutant mouse nerve using immunohistochemistry and electron microscopy (data not shown). This suggests that impaired mitochondrial fusion has no overt effect on myelination. However 20 weeks later signs of axonal degeneration and demyelination were observed in the sciatic of these mice (Fig. 5e) (Sarzi et al., 2012), showing that fusion impairment is nevertheless detrimental to long term peripheral neuron survival and myelin sheath maintenance. Our observations further highlight the importance of functional glial mitochondria for survival of peripheral neurons (Viader et al., 2013).

We demonstrate that the labeling of mitochondria with a virally-expressed fluorescent probe combined with the imaging of the sciatic nerve of living mice with a multiphoton microscope enables thorough in situ and in vivo study of mitochondrial dynamics with relevant quantifications of physical parameters for up to five hours. Importantly in vivo mitochondria dynamics and morphology can be

used as mitochondrial biomarker for OPA1 disease and probably for other neurodegenerative diseases. This approach preserves mitochondrial physiology in a relevant in vivo context avoiding the common artifacts that result from fixation, staining or non-physiological cell culture conditions. Moreover it allows a direct evaluation of drug effects on mitochondrial dynamics, as well as the characterization of mutations in genes encoding mitochondrial proteins in a timely manner. With the increasing focus on the role of mitochondria across many neurodegenerative diseases (Burté et al., 2015), we believe that this method will be helpful to decipher both pathological changes and therapeutic effects on mitochondrial physiology in myelin in vivo.

Supplementary data to this article can be found online at <http://dx.doi.org/10.1016/j.mito.2015.05.004>.

Acknowledgments

We acknowledge H. Boukhadaoui (Montpellier RIO Imaging Platform), C. Cazeville and A. Caballero-Megido (CRIC - TEM Platform), the RHEM platform and the Animal Facility of the INM for help and technical assistance. This work was supported by the European Research Council grant (FP7-IDEAS-ERC 311610) and an INSERM – AVENIR grant.

References

- Amati-Bonneau, P., Pasquier, L., Lainey, E., et al., 2005. Sporadic optic atrophy due to synonymous codon change altering mRNA splicing of OPA1. *Clin. Genet.* 67 (1), 102–103.
- Amati-Bonneau, P., Valentino, M.L., Reynier, P., Gallardo, M.E., et al., 2008. OPA1 mutations induce mitochondrial DNA instability and optic atrophy 'plus' phenotypes. *Brain* 131 (Pt 2), 338–351.
- Amati-Bonneau, P., Milea, D., Bonneau, D., et al., 2009. OPA1-associated disorders: phenotypes and pathophysiology. *Int. J. Biochem. Cell Biol.* 41 (10), 1855–1865.
- Belenguer, P., Pellegrini, L., 2013. The dynamin GTPase OPA1: more than mitochondria? *Biochim. Biophys. Acta* 1833 (1), 176–183.
- Bereiter-Hahn, J., Vöth, M., 1994. Dynamics of mitochondria in living cells: shape changes, dislocations, fusion, and fission of mitochondria. *Microsc. Res. Tech.* 27 (3), 198–219.
- Berthold, C.H., Rydmark, M., 1995. Morphology of normal peripheral axons. Chapter in the book *The Axon: Structure, Function, and Pathophysiology* published by Stephen G. Waxman, Jeffery D. Kocsis, Peter K. Stys. Oxford University Press.
- Bonneau, D., Colin, E., Florine Oca, F., Marc Ferré, M., Chevrollier, A., et al., 2014. Early-onset Behr syndrome due to compound heterozygous mutations in OPA1. *Brain* 137 (Pt 10), e301.
- Burté, F., Carelli, V., Chinnery, P.F., Yu-Wai-Man, P., 2015. Disturbed mitochondrial dynamics and neurodegenerative disorders. *Nat. Rev. Neurol.* 11 (1), 11–24.
- Cai, Q., Davis, M.L., Sheng, Z.H., 2011. Regulation of axonal mitochondrial transport and its impact on synaptic transmission. *Neurosci. Res.* 70, 9–15.
- Cartoni, R., Martinou, J.C., 2009. Role of mitofusin 2 mutations in the physiopathology of Charcot-Marie-Tooth disease type 2A. *Exp. Neurol.* 218 (2), 268–273.
- Cassereau, J., et al., 2011. Mitochondrial dysfunction and pathophysiology of Charcot-Marie-Tooth disease involving GDAP1 mutations. *Exp. Neurol.* 227 (1), 31–41.
- Christensen, D.J., Nedergaard, M., 2011. Two-photon in vivo imaging of cells. *Pediatr. Nephrol.* 26, 1483–1489.
- Cornblath, D.R., Hoke, A., 2006. Recent advances in HIV neuropathy. *Curr. Opin. Neurol.* 19 (5), 446–450.
- Cotter, L., et al., 2010. Dlg1-PTEN interaction regulates myelin thickness to prevent damaging peripheral nerve overmyelination. *Science* 328, 1415–1418.
- de Moura, M.B., dos Santos, L.S., Van Houten, B., 2010. Mitochondrial dysfunction in neurodegenerative diseases and cancer. *Environ. Mol. Mutagen.* 51 (5), 391–405.
- Delettre, C., Lenaers, G., Griffoin, J.M., et al., 2000. Nuclear gene OPA1, encoding a mitochondrial dynamin-related protein, is mutated in dominant optic atrophy. *Nat. Genet.* 26 (2), 207–210.
- Edgar, J.M., McCulloch, M.C., Thomson, C.E., Griffiths, I.R., 2008. Distribution of mitochondria along small-diameter myelinated central nervous system axons. *J. Neurosci. Res.* 86 (10), 2250–2257.
- Einheber, S., Bhat, M.A., Salzer, J.L., 2006. Disrupted axo-glial junctions result in accumulation of abnormal mitochondria at nodes of ranvier. *Neuron Glia Biol.* 2 (3), 165–174.
- Elachouri, G., Vidoni, S., Zanna, C., Pattyn, A., Boukhadaoui, H., et al., 2011. OPA1 links human mitochondrial genome maintenance to mtDNA replication and distribution. *Genome Res.* 21 (1), 12–20.
- Eshed-Eisenbach, Y., Peles, E., 2013. The making of a node: a co-production of neurons and glia. *Curr. Opin. Neurobiol.* 23 (6), 1049–1056.
- Feldman, D., Anderson, T.D., 1994. Schwann cell mitochondrial alterations in peripheral nerves of rabbits treated with 2',3'-dideoxycytidine. *Acta Neuropathol.* 87 (1), 71–80.
- Frezza, C., Cipolat, S., Martins de Brito, O., Micaroni, M., et al., 2006. OPA1 controls apoptotic cristae remodeling independently from mitochondrial fusion. *Cell* 126 (1), 177–189.

- Gonzalez, S., Fernando, R., Perrin-Tricaud, C., Tricaud, N., 2014. In vivo introduction of transgenes into mouse sciatic nerve cells in situ using viral vectors. *Nat. Protoc.* 9 (5), 1160–1169.
- He, T.C., Zhou, S., da Costa, L.T., Yu, J., Kinzler, K.W., Vogelstein, B., 1998. A simplified system for generating recombinant adenoviruses. *Proc. Natl. Acad. Sci. U. S. A.* 95 (5), 2509–2514.
- Hirata, N., Shim, Y.H., Pravdic, D., et al., 2011. Isoflurane differentially modulates mitochondrial reactive oxygen species production via forward versus reverse electron transport flow: implications for preconditioning. *Anesthesiology* 115 (3), 531–540.
- Kabzińska, D., Kotruchow, K., et al., 2014. A severe recessive and a mild dominant form of Charcot–Marie–Tooth disease associated with a newly identified Glu222Lys GDAP1 gene mutation. *Acta Biochim. Pol.* 61 (4), 739–744.
- Lardy, H.A., 1980. Antibiotic inhibitors of mitochondrial energy transfer. *Pharmacol. Ther.* 11 (3), 649–660.
- Legros, F., et al., 2002. Mitochondrial fusion in human cells is efficient, requires the inner membrane potential, and is mediated by mitofusins. *Mol. Biol. Cell* 13 (12), 4343–4354.
- Lodi, R., Tonon, C., Valentino, M.L., Lotti, S., et al., 2004. Deficit of in vivo mitochondrial ATP production in OPA1-related dominant optic atrophy. *Ann. Neurol.* 56 (5), 719–723.
- Marchant, J.S., Stutzmann, G.E., Leissring, M.A., LaFerla, F.M., Parker, I., 2001. Multiphoton-evoked color change of DsRed as an optical highlighter for cellular and subcellular labeling. *Nat. Biotechnol.* 19 (7), 645–649.
- Misgeld, T., et al., 2007. Imaging axonal transport of mitochondria in vivo. *Nat. Methods* 4 (7), 559–561.
- Ohno, N., et al., 2011. Myelination and axonal electrical activity modulate the distribution and motility of mitochondria at CNS nodes of Ranvier. *J. Neurosci.* 31 (20), 7249–7258.
- Okada, T., et al., 2009. Scalable purification of adeno-associated virus serotype 1 (AAV1) and AAV8 vectors, using dual ion-exchange adsorptive membranes. *Hum. Gene Ther.* 20 (9), 1013–1021.
- Olichon, A., Baricault, L., Gas, N., et al., 2003. Loss of OPA1 perturbs the mitochondrial inner membrane structure and integrity, leading to cytochrome c release and apoptosis. *J. Biol. Chem.* 278 (10), 7743–7746.
- Ozçelik, M., Cotter, L., et al., 2010. Pals1 is a major regulator of the epithelial-like polarization and the extension of the myelin sheath in peripheral nerves. *J. Neurosci.* 30 (11), 4120–4131.
- Romanelli, E., et al., 2013. Cellular, subcellular and functional in vivo labeling of the spinal cord using vital dyes. *Nat. Protoc.* 8 (3), 481–490.
- Sarzi, E., Angebault, C., Seveno, M., et al., 2012. The human OPA1^{deITTAG} mutation induces premature age-related systemic neurodegeneration in mouse. *Brain* 135 (Pt 12), 3599–3613.
- Schroder, J.M., 1993. Neuropathy associated with mitochondrial disorders. *Brain Pathol.* 3 (2), 177–190.
- Stefanini, M., De Martino, C., Zamboni, L., 1967. Fixation of ejaculated spermatozoa for electron microscopy. *Nature* 216, 173–174.
- Tricaud, N., Perrin-Tricaud, C., Brusés, J.L., Rutishauser, U., 2005. Adherens junctions in myelinating Schwann cells stabilize Schmidt–Lanterman incisures via recruitment of p120 catenin to E-cadherin. *J. Neurosci.* 25 (13), 3259–3269.
- Viader, A., et al., 2013. Aberrant Schwann cell lipid metabolism linked to mitochondrial deficits leads to axon degeneration and neuropathy. *Neuron* 77 (5), 886–898.
- Yu-Wai-Man, P., Griffiths, P.G., et al., 2010. Multi-system neurological disease is common in patients with OPA1 mutations. *Brain* 133 (Pt 3), 771–786.
- Zhang, C.L., et al., 2010. Activity-dependent regulation of mitochondrial motility by calcium and Na/K-ATPase at nodes of Ranvier of myelinated nerves. *J. Neurosci.* 30 (10), 3555–3566.
- Zonta, B., Tait, S., Melrose, S., et al., 2008. Glial and neuronal isoforms of Neurofascin have distinct roles in the assembly of nodes of Ranvier in the central nervous system. *J. Cell Biol.* 181 (7), 1169–1177.